

LETTER • OPEN ACCESS

Enhanced Asian warming increases Arctic amplification

To cite this article: Yongkun Xie *et al* 2023 *Environ. Res. Lett.* **18** 034041

View the [article online](#) for updates and enhancements.

You may also like

- [Warm Arctic cold Siberia: comparing the recent and the early 20th-century Arctic warmings](#)

Martin Wegmann, Yvan Orsolini and Olga Zolina

- [Atmospheric circulation patterns which promote winter Arctic sea ice decline](#)

Binhe Luo, Dehai Luo, Lixin Wu *et al.*

- [Summer Russian heat waves and their links to Greenland's ice melt and sea surface temperature anomalies over the North Atlantic and the Barents–Kara Seas](#)

Hejing Wang and Dehai Luo



Breath Biopsy® OMNI®

The most advanced, complete solution for global breath biomarker analysis

TRANSFORM YOUR
RESEARCH WORKFLOW



Expert Study Design & Management



Robust Breath Collection



Reliable Sample Processing & Analysis



In-depth Data Analysis



Specialist Data Interpretation

ENVIRONMENTAL RESEARCH
LETTERS

OPEN ACCESS

RECEIVED
17 November 2022REVISED
14 February 2023ACCEPTED FOR PUBLICATION
21 February 2023PUBLISHED
7 March 2023

Original content from this work may be used under the terms of the Creative Commons Attribution 4.0 licence.

Any further distribution of this work must maintain attribution to the author(s) and the title of the work, journal citation and DOI.



LETTER

Enhanced Asian warming increases Arctic amplification

Yongkun Xie¹, Jianping Huang^{1,*}, Guoxiong Wu^{2,3}, Nan Lei^{1,4} and Yimin Liu^{2,3}¹ Collaborative Innovation Center for Western Ecological Safety, Lanzhou University, Lanzhou, People's Republic of China² State Key Laboratory of Numerical Modeling for Atmospheric Sciences and Geophysical Fluid Dynamics (LASG), Institute of Atmospheric Physics, Chinese Academy of Sciences, Beijing, People's Republic of China³ College of Earth and Planetary Sciences, University of Chinese Academy of Sciences, Beijing, People's Republic of China⁴ College of Atmospheric Sciences, Lanzhou University, Lanzhou, People's Republic of China

* Author to whom any correspondence should be addressed.

E-mail: hjp@lzu.edu.cn**Keywords:** Asian warming, Arctic amplification, Tibetan Plateau, dryland, Barents–Kara SeasSupplementary material for this article is available [online](#)

Abstract

The Arctic has been experiencing prominent warming amplification. However, despite anthropogenic emissions and oceanic variability, whether Arctic amplification has a connection with land in the lower latitudes remains unknown. Here, we newly identify enhanced Asian warming as a factor underlying Arctic amplification. The simulations demonstrate that enhanced Asian warming contributes 22% of the wintertime amplified warming over the Barents–Kara Seas (BKS). We demonstrate that Asian warming remotely affects the Arctic by affecting poleward atmospheric heat and moisture transport. The external anomalous heat and moisture further trigger local feedbacks concerning sea ice-albedo feedback and changes in longwave radiation and evaporation, thus facilitating BKS warming amplification. The capacitor effect of the Arctic Ocean further modulates the seasonality of BKS warming via turbulent heat flux exchange between the atmosphere and ocean. Moreover, anomalous Rossby wave trains are responsible for the anomalous atmospheric circulations favoring the atmospheric heat and moisture transport into BKS. Our findings illuminate a new factor from remote lower latitudes affecting Arctic climate change.

1. Introduction

The Arctic, especially the Barents–Kara Seas (BKS), has been experiencing the strongest warming on Earth, which is often called Arctic amplification (Screen and Simmonds 2010, Stouffer and Manabe 2017, IPCC 2021). This warming amplification originates from anthropogenic emissions (Gillett *et al* 2008, Pithan and Mauritsen 2014, Stouffer and Manabe 2017) and is regulated by local feedbacks (Screen and Simmonds 2010, Pithan and Mauritsen 2014, Dai *et al* 2019, Gao *et al* 2019, Xie *et al* 2019) and external heat and moisture transport (Cai 2005, Lu and Cai 2009, Delworth *et al* 2016, Graversen and Burtu 2016, You *et al* 2021).

The local feedbacks influence the Arctic warming by modifying the atmospheric and oceanic energy balance. For example, the sea ice-albedo feedback in summer favors the Arctic warming in winter via absorbing energy in summer and releasing energy in winter (Boeke and Taylor 2018, Xie *et al* 2022a). The

enhanced downward longwave (LW) radiation associated with atmospheric moisture is also suggested to contribute to Arctic warming (Lu and Cai 2009, Gao *et al* 2019, Lesins *et al* 2012). The atmospheric moisture is further influenced by the external moisture transport from lower latitudes (Cai 2005, Graversen and Burtu 2016, Luo *et al* 2017, Cai *et al* 2022). In addition, external heat transport to the Arctic can directly increase Arctic warming (Delworth *et al* 2016, You *et al* 2021). On interdecadal time scales, Arctic climate change is also modulated by the internal climate variability associated with oceans (Delworth *et al* 2016, Ding *et al* 2018, Svendsen *et al* 2018). The influence of Arctic climate change on the mid-latitudes has been widely studied (Kretschmer *et al* 2016, Blackport *et al* 2019, Cohen *et al* 2019, Xie *et al* 2020). Meanwhile, studies have also suggested an influence of mid-latitudes on the Arctic (Luo *et al* 2017, Cai *et al* 2022, Xie *et al* 2022b). However, the influence from land, especially the remote regions in lower latitudes, has not been investigated.

Enhanced Asian warming has been demonstrated to be prominent over the land (Huang *et al* 2012, Xie *et al* 2019, Yao *et al* 2019). This enhanced warming mainly includes two parts, enhanced warming in the Asian dryland (Huang *et al* 2016a, 2017) and enhanced warming over the Tibetan Plateau (Duan and Xiao 2015, You *et al* 2020). The warming magnitude over the global dryland during the last century is 20%–40% larger than that over the global humid regions (Huang *et al* 2017). The warming over the Tibetan Plateau was 1.8 times the global mean warming during the period from 1979 to 2020 (You *et al* 2021). However, the Asian dryland and elevation higher than 500 m domains overlap vastly (figure S1). Hence, in this study, the effect of enhanced Asian warming was simulated by halving the sensible heat (SH) (vertical diffusive heat) over the Asian land higher than 500 m (AL500-sh0.5).

The influence of the warming over the Asian dryland and Tibetan Plateau on the remote Arctic climate has not been investigated, although the climatic effect of Tibetan Plateau heating on mid-latitude regions across the Northern Hemisphere has been widely recognized (Yanai *et al* 1992, Liu *et al* 2007, Wu *et al* 2012, Lu *et al* 2018, Yang *et al* 2020). Therefore, it is important to explore whether the Tibetan Plateau heating can exert an additional influence on the Arctic, aside from the influence on mid-latitudes. Moreover, the climatic effect of dryland warming needs to be investigated urgently given the threat of persistently expanding and warming dryland in the future (Feng and Fu 2013, Huang *et al* 2016b, 2017).

2. Data and methods

2.1. Data

The observational temperature was based on the ERA5 reanalysis data provided by ECMWF (Hersbach *et al* 2020) in $1^\circ \times 1^\circ$ grids from 1950 to the present. The observational precipitation and potential evapotranspiration datasets were based on the Climatic Research Unit (CRU) TS version 4.05 data (Harris *et al* 2020) in $0.5^\circ \times 0.5^\circ$ grids from 1901 to 2020. The dryland classification was based on the aridity index calculated as annual precipitation divided by potential evapotranspiration (Feng and Fu 2013, Huang *et al* 2016a). In addition, the aridity index data provided by Feng and Fu (2013) were used. This aridity index was calculated from the NOAA's Precipitation Reconstruction over Land (PREC/L) (Chen *et al* 2002) and Global Land Data Assimilation System specific humidity, solar radiations, and wind speed (Rodell *et al* 2004) in $0.5^\circ \times 0.5^\circ$ grids from 1948 to 2008. The potential evapotranspiration for both datasets was calculated using the Penman–Monteith algorithm (Allen *et al* 1998). Although the subtypes of the dryland were different in some regions, such as hyper-arid and arid regions, the overall Asian dryland

domains agreed well between the two datasets (figure S1). Therefore, the dryland classification was reliable.

2.2. Numerical simulations and models

We performed two series of numerical experiments using the Community Earth System Model (CESM) (table S1; Danabasoglu *et al* 2020): the halving-SH (sh0.5) and the non-SH (nosh) experiments, which were developed from the benchmark experiments of the Global Monsoons Model Intercomparison Project (GMMIP) (Zhou *et al* 2016) of the Coupled MIP Phase 6 (CMIP6) (Eyring *et al* 2016). The sh0.5 and nosh experiments were fully coupled and atmosphere-only simulations (amips), respectively. In this study, the sh0.5 experiment was mainly examined, and the nosh experiment was a supportive experiment that was used to verify the reliability of the CESM model and the reasonableness of the experimental designs. The control runs of the sh0.5 and nosh experiments were historical (HIST) simulations of CMIP6 labeled as HIST and amip-HIST, respectively, where amip indicates atmosphere-only simulation. The sensitivity runs of the sh0.5 and nosh experiments were designed as halving or removing the SH over Asian land above 500 m (AL500), labeled as AL500-sh0.5 and amip-AL500-nosh, respectively. In this study, SH indicates the vertical diffusive heat from the surface to the top of the atmosphere (Wu *et al* 2007, Xie *et al* 2023) rather than just SH flux at the surface.

Because the nosh experiment was the benchmark experiment of GMMIP (table S1), nosh experiments were also available for two models participating in GMMIP: FGOALS-f3-L (He *et al* 2020) and FIO-ESM-2-0 (Bao *et al* 2020). Therefore, a comparison of the results from CESM with those from CMMIP can verify the performance of CESM in SH-modification experiments. The details of the models are introduced in table S1. Although the amip-HIST of GMMIP has three ensemble integrations, the amip-AL500-nosh of GMMIP has only one integration, so only one integration was examined. The integration periods for the nosh experiments of CESM and GMMIP were from 1979/01 to 2014/12 and 1870/01 to 2014/12, respectively. Therefore, the period from 1979/01 to 2014/12 was analyzed for nosh experiments. In addition, the period from 1850/01 to 2014/12 was analyzed for sh0.5 experiments.

The performance of CESM in simulating the basic climate elements was addressed as follows: the control run could reproduce the climate in the observations (figure S2), ensuring the basis for further analyses of the sensitivity run. Specifically, the control run well simulated the climatological near-surface air temperature distributions and seasonality from the subtropics to the Arctic, including our target AL500 and BKS domains (figures S2(a)–(d)); some observed small-scale features were lacking in simulations because the horizontal resolution of CESM was lower than

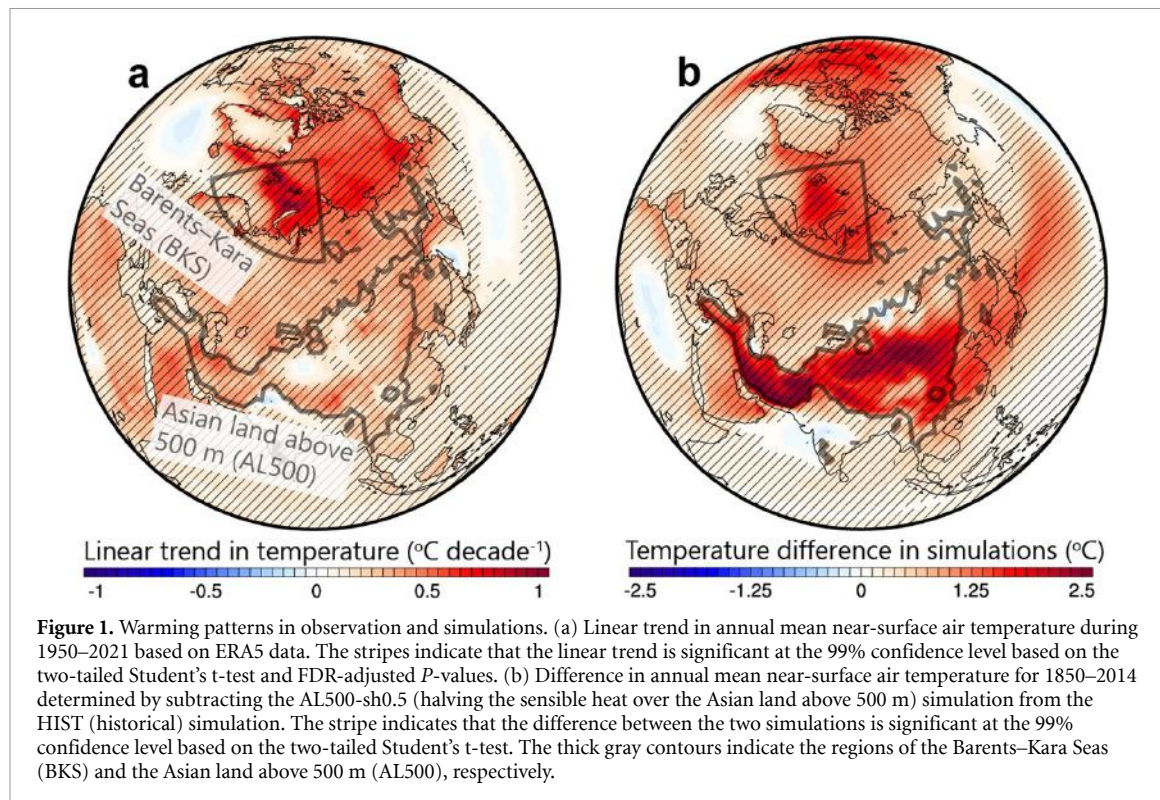


Figure 1. Warming patterns in observation and simulations. (a) Linear trend in annual mean near-surface air temperature during 1950–2021 based on ERA5 data. The stripes indicate that the linear trend is significant at the 99% confidence level based on the two-tailed Student's t-test and FDR-adjusted P -values. (b) Difference in annual mean near-surface air temperature for 1850–2014 determined by subtracting the AL500-sh0.5 (halving the sensible heat over the Asian land above 500 m) simulation from the HIST (historical) simulation. The stripe indicates that the difference between the two simulations is significant at the 99% confidence level based on the two-tailed Student's t-test. The thick gray contours indicate the regions of the Barents–Kara Seas (BKS) and the Asian land above 500 m (AL500), respectively.

the resolution of ERA5. In addition, the atmospheric circulations were well simulated in the control run, as indicated by the geopotential height at 500 hPa (figures S2(e)–(h)). For example, the extratropical troughs and ridges were identical between simulations and observations. The geopotential height was higher in the tropics in simulations than in observations, which probably occurred because the vertical resolution of CESM was lower than that of ERA5, specifically, 32 and 137 vertical levels for CESM and ERA5, respectively (Danabasoglu *et al* 2020, Hersbach *et al* 2020).

The considerations underlying the SH-modification experiments were addressed as follows: (i) Two typical methods can be used to modify temperature over land, namely modifications in surface albedo (Wang *et al* 2008, Lu *et al* 2018) and SH (Wu *et al* 2007, Zhou *et al* 2016). (ii) SH is the major component of total heating over the Tibetan Plateau (Yanai *et al* 1992, Wu *et al* 2007) and Asian dryland (Huang *et al* 2017, Xie *et al* 2019). Consequently, modifying SH can directly modify the major parts of total heating. Because modifying albedo indirectly changes total heating via multiple feedbacks, total heating changes induced by modifying albedo are complicated. Therefore, we followed the GMMIP method to modify SH. (iii) The benchmark nosh experiments generated strong warming, approximately 4.5 °C averaged over AL500 (figure S3). Therefore, we redesigned the sensitivity experiment by halving, instead of removing, the SH. The sh0.5 experiment had a 1.5 °C warming (figure 1(b)),

which was less than the observed 1.9 °C accumulated warming magnitude of AL500 from 1950 to 2021 (figure 1(a)). In addition, for a fair comparison with observation, the results based on sensitivity experiments were further scaled to observation, as introduced in section 2.3.

The technical details of the SH-modification experiments were addressed as follows: (i) The SH was not prescribed to a predetermined value but was modified in each time step of model integration; thus, all feedbacks were completely active. (ii) For attribution of the influence of sea surface temperature variation, pacemaker experiments performed by restoring the sea surface temperature to observed values have been widely used (Kosaka and Xie 2013, Zhou *et al* 2016). However, the temperature of the atmosphere is a predict and of the atmospheric circulation model, instead of the variables, such as sea surface temperature, that are communicated among the components of the model through the coupler. Therefore, the restoring method used for sea surface temperature was not suitable for the temperature of the atmosphere. (iii) The modification was not limited to the single-level SH flux exchange between the land surface and atmosphere but was on the entire column of the atmosphere; that is, the halving or removing of the SH (vertical diffusive heat) was done in all model levels of the atmosphere. The practice of modifying the entire atmosphere was implemented to assure the vertical continuity of total heating of the atmosphere. (iv) In coding, the SH (variable 'cam_in%shf' in CESM codes) in all model levels of the atmosphere

over the AL500 regions was multiplied by 0.5 for the sh0.5 experiment or zero for the nosh experiment, in each time step of the model integration. Refer to the Data availability statement for our codes regarding CESM experiments. (v) Because the feedbacks are completely active in the simulations, the energy conservation in the model after halving SH was established by the instant adjustment in each time step of the model integration, such as the decrease in LW cooling which was directly indicated by the temperature changes (figure S4(a)). In addition, because the diffusive SH generally decays with height, halving SH mainly changes the SH in the lower troposphere over the AL500 (Wu *et al* 2007).

The effects of halving SH on basic variables of local climate were addressed as follows: The warming induced by halving SH occurred from the surface through the entire troposphere over AL500 (figure S4(a)), which was consistent with the observations (figure S4(b)). In addition, the greenhouse gas-induced HIST warming from 1861 to 2004 over the dryland shows a prominent increase in SH at the surface (Xie *et al* 2019). Despite decadal variability due to near-surface wind variation, the surface SH over the Tibetan Plateau was also suggested to increase with long-term warming (Wang *et al* 2019). Therefore, halving SH simulation can reasonably represent the warming over AL500 shown in observations. Furthermore, the high consistency in the differences in temperature, precipitation, and geopotential height at 500 hPa of the nosh experiment between CESM and GMMIP suggests that the SH-modification simulations of CESM model were reliable (figure S3). The warming over AL500 in the nosh experiment (figures S3(a) and (b)) showed similar patterns but stronger magnitudes than the warming in the sh0.5 experiment (figure 1(b)). The differences in the atmosphere-only nosh experiment were not statistically significant in the Arctic, which suggests that air-sea interactions were crucial for the Asia and Arctic connections in the sh0.5 experiment. Although only SH was modified, the latent heat (LH) due to precipitation (figures S3(c) and (d)) also changed in the SH-modification experiments because of feedback (Wu *et al* 2016). Therefore, the climate impact in the SH-modification experiments was induced not only by SH but also by the pertinent feedbacks.

In the analysis, the differences determined using HIST minus AL500-sh0.5 indicate the influence of Asian warming. Because the AL500-sh0.5 experiment was not a pacemaker experiment, the 1850–2014 mean differences between control and sensitivity runs were analyzed as the general sensitivity experiments, instead of analyzing the trends as with pacemaker experiments (Kosaka and Xie 2013). The 165 year average was sufficient to eliminate the influence of internal climate variability. For example, the Pacific Decadal Oscillation and Atlantic Multi-decadal Oscillation have long periods of only 50–70

and 50–80 years (Mantua and Hare 2002, Lin *et al* 2019), respectively. The benchmark time-slice experiments of the Polar Amplification Model Intercomparison Project (PAMIP), which aims to investigate Arctic climate change, adopted 100 ensemble integrations, where the time-slice experiments perform a one-year integration each time and repeat many times (Smith *et al* 2019). Consequently, the 100 ensemble integrations of PAMIP were equal to the 100 year integrations of our experiments. Therefore, although only one integration was performed in our experiment, the 165 year integration assures the reliability of the simulations. Although the influence of internal climate variability on sensitivity experiments was mostly eliminated by the experimental designs in this study, internal climate variability was crucial for the observed trends over a decadal timescale (Kosaka and Xie 2013, Trenberth 2015).

2.3. Diagnostic methods

To compare the results of the sensitivity experiment with observations, the temperature differences in the simulations should be scaled to the warming trend based on the sensitivity of response to forcing, namely, the BKS temperature change (T_{BKS}) in response to the AL500 temperature change (T_{AL500}) in the sh0.5 experiment. Specifically, the temperature difference in the simulations (T^S) was scaled to the warming trend in the observation (T^O), according to the formulation $T_{\text{Scaled}} = \frac{T^S_{\text{BKS}}}{T^S_{\text{AL500}}} \times T^O_{\text{AL500}}$, where T_{Scaled} indicates the warming trend ($^{\circ}\text{C decade}^{-1}$) in the simulations after scaling and $\frac{T^S_{\text{BKS}}}{T^S_{\text{AL500}}}$ indicates the response-to-forcing ratio in the simulations. The formulation physically means that the scaled BKS warming was the product of the simulated response-to-forcing ratio and the observed changes in forcing. The forcing of AL500 warming had a cross-season influence on the BKS temperature response (section 3.2) because of the cross-season energy cycles in the BKS (Boeke and Taylor 2018, Xie *et al* 2022a). Therefore, T^S_{AL500} and T^O_{AL500} used annual mean values, while T^S_{BKS} used monthly mean values. The values of T^S_{AL500} and T^O_{AL500} were 1.51°C and $0.26^{\circ}\text{C decade}^{-1}$, respectively (figure 1). To quantify the amplified warming of AL500 and BKS relative to the global mean, the global mean warming values (T^O_{Global}) were further removed when calculating the contribution rate of enhanced Asian warming to BKS warming amplification; namely, the formulation of the contribution rate was $\frac{T^S_{\text{BKS}}/T^S_{\text{AL500}} \times (T^O_{\text{AL500}} - T^O_{\text{Global}})}{T^O_{\text{BKS}} - T^O_{\text{Global}}} \times 100$.

The local energy budget at the sea surface of the Arctic Ocean was formulated as

$$E_{\text{net}}^{\downarrow} = \underbrace{SW^{\downarrow} - SW^{\uparrow}}_{SW_{\text{net}}^{\downarrow}} + \underbrace{LW^{\downarrow} - LW^{\uparrow}}_{LW_{\text{net}}^{\downarrow}} - \underbrace{(SH^{\uparrow} + LH^{\uparrow})}_{TH^{\uparrow}},$$

where $E_{\text{net}}^{\downarrow}$ is the net energy uptake due to local absorption by seawater and external horizontal

oceanic heat transport and $SW_{\text{net}}^{\downarrow}$ and $LW_{\text{net}}^{\downarrow}$ indicate the net shortwave (SW) and LW radiation at the sea surface, respectively. TH^{\uparrow} indicates the upward turbulent heat (TH) flux, which is the sum of SH and LH. In an alternative form, the budget of upward LW radiation is $LW^{\uparrow} = SW_{\text{net}}^{\downarrow} + LW^{\downarrow} - TH^{\uparrow} - E_{\text{net}}^{\downarrow}$. In addition, the net SW solar radiation change can be decomposed as the sum of contributions by albedo feedback and downward SW solar radiation (SW^{\downarrow}) change as follows:

$$\delta(SW_{\text{net}}^{\downarrow}) \approx \underbrace{\delta(1 - \alpha)SW^{\downarrow}}_{\text{Albedo feedback}} + \underbrace{(1 - \alpha)\delta(SW^{\downarrow})}_{\text{SW}^{\downarrow} \text{ change}},$$

where the operator δ indicates the HIST minus AL500-sh0.5 difference and $\alpha = \frac{SW^{\uparrow}}{SW^{\downarrow}}$ is the surface albedo. The formulations $SW^{\uparrow} = \alpha SW^{\downarrow}$ and $SW_{\text{net}}^{\downarrow} = (1 - \alpha)SW^{\downarrow}$ were introduced.

The horizontal heat flux was expressed as $\vec{H} = \rho \vec{V} \theta$, where ρ , \vec{V} , and θ indicate the density, horizontal velocity, and potential temperature of the atmosphere, respectively. The vertical integral of \vec{H} is calculated according to formulation $\{\vec{H}\} = \int_0^{\infty} \vec{H} dz = \int_0^{\infty} \rho \vec{V} \theta dz = -\frac{1}{g} \int_{p_s}^0 \vec{V} \theta dp$, where g , p , and p_s indicate the acceleration of gravity, pressure, and surface pressure, respectively. The horizontal moisture flux is $\vec{M} = \rho \vec{V} q$, where q indicates specific humidity. The vertical integral of \vec{M} is $\{\vec{M}\} = \int_0^0 \vec{M} dz = \int_0^0 \rho \vec{V} q dz = -\frac{1}{g} \int_0^{p_s} \vec{V} q dp$. Because the fluxes are non-linear, we calculated the heat and moisture fluxes using the three-hourly output for the period from 2000 to 2014; only 15 years of high-frequency outputs were available because high-frequency outputs cost large storage. Furthermore, the eddy stream function and Plumb wave activity flux were used to examine the stationary Rossby wave trains. The eddy stream function means that the zonal mean of the stream function was removed. The Plumb wave activity flux was calculated based on the formula (7.1) in Plumb (1985).

2.4. Statistical analysis

The linear trend for the period from 1950 to 2021 was calculated using linear regression based on the least square method, and its statistical significance was estimated using a two-tailed Student's t-test and the false discovery rate (FDR)-adjusted P -values (P_{adj}), namely, $P_{\text{adj}} < 0.01$ for the 99% confidence level. The FDR method was used to enhance the reliability of statistical significance when the linear trends were analyzed on a spatial map (Benjamini and Hochberg 1995). FDR-adjusted P -values were formulated as $P_{\text{adj}} = P \times [N/\text{Rank}(P)]$, where N indicates the total number of grids on the map and $\text{Rank}(P)$ indicates the rank of P starting from 1 when all P -values were sorted in ascending order. In addition, the statistical significance (99% confidence level, $P < 0.01$) of the

difference between the control run and sensitivity run was estimated using a two-tailed Student's t-test.

3. Results

3.1. Contribution of enhanced Asian warming to Arctic warming

The linear trend in annual mean near-surface air temperature during 1950–2021 demonstrates that Arctic warming was the strongest over the BKS (figure 1(a)). This BKS warming amplification has been widely suggested by observations and simulations (Gillett *et al* 2008, Screen and Simmonds 2010, Pithan and Mauritsen 2014, Stouffer and Manabe 2017, Dai *et al* 2019, Xie *et al* 2019, IPCC 2021). In this study, the difference between the control run (HIST) and the sensitivity run (AL500-sh0.5; halving the SH over Asian land above 500 m), i.e. HIST minus AL500-sh0.5, indicates the influence of Asian warming (section 2.2). As in the observations, the Asian warming in the simulations was not only at the surface but also in the entire troposphere (figure S4). The simulations demonstrate that Asian warming significantly (99% confidence level) contributed to both the overall Arctic warming and the BKS warming amplification (figure 1(b)). Given that the influence on BKS amplification was the most prominent in the simulations, the influence of Asian warming on BKS warming was focused on.

Arctic amplification is characterized by strong seasonality (Lu and Cai 2009, Pithan and Mauritsen 2014, Stouffer and Manabe 2017, Dai *et al* 2019, Xie *et al* 2019). The seasonality of the BKS warming in the simulations after scaling (section 2.3; red line) was consistent with the observation (black line) (figure 2(a)). BKS warming was much stronger in winter than in summer, so BKS warming amplification was observed in the cold season from late autumn to early spring but not observed in the summer (Lu and Cai 2009, Pithan and Mauritsen 2014). The amplified BKS warming relative to the global mean was further quantified by removing the global mean warming trend from BKS warming (section 2.3).

The enhanced Asian warming-induced BKS warming in the simulations accounted for a large portion of the observed BKS warming amplification (figure 2(b)). Specifically, the results demonstrate that enhanced Asian warming contributed 25% of the annual mean BKS warming amplification in the observation (figure 2(b)). The contribution rate was higher in summer because the observed BKS warming was weak and almost not amplified relative to the global mean. Thus, the wintertime BKS warming amplification was focused on. In the cold season, when BKS warming amplification was most prominent, the contribution of enhanced Asian warming was 22%. Therefore, Asian warming exerted a crucial influence on BKS warming amplification.

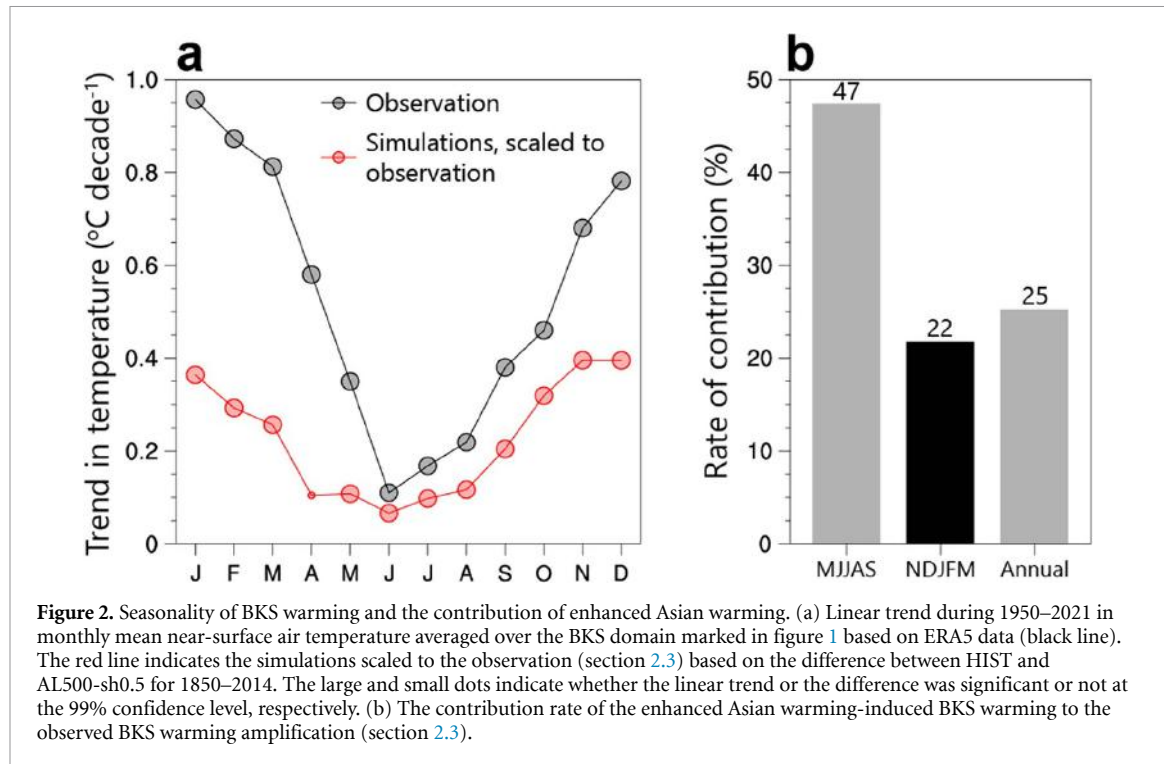


Figure 2. Seasonality of BKS warming and the contribution of enhanced Asian warming. (a) Linear trend during 1950–2021 in monthly mean near-surface air temperature averaged over the BKS domain marked in figure 1 based on ERA5 data (black line). The red line indicates the simulations scaled to the observation (section 2.3) based on the difference between HIST and AL500-sh0.5 for 1850–2014. The large and small dots indicate whether the linear trend or the difference was significant or not at the 99% confidence level, respectively. (b) The contribution rate of the enhanced Asian warming-induced BKS warming to the observed BKS warming amplification (section 2.3).

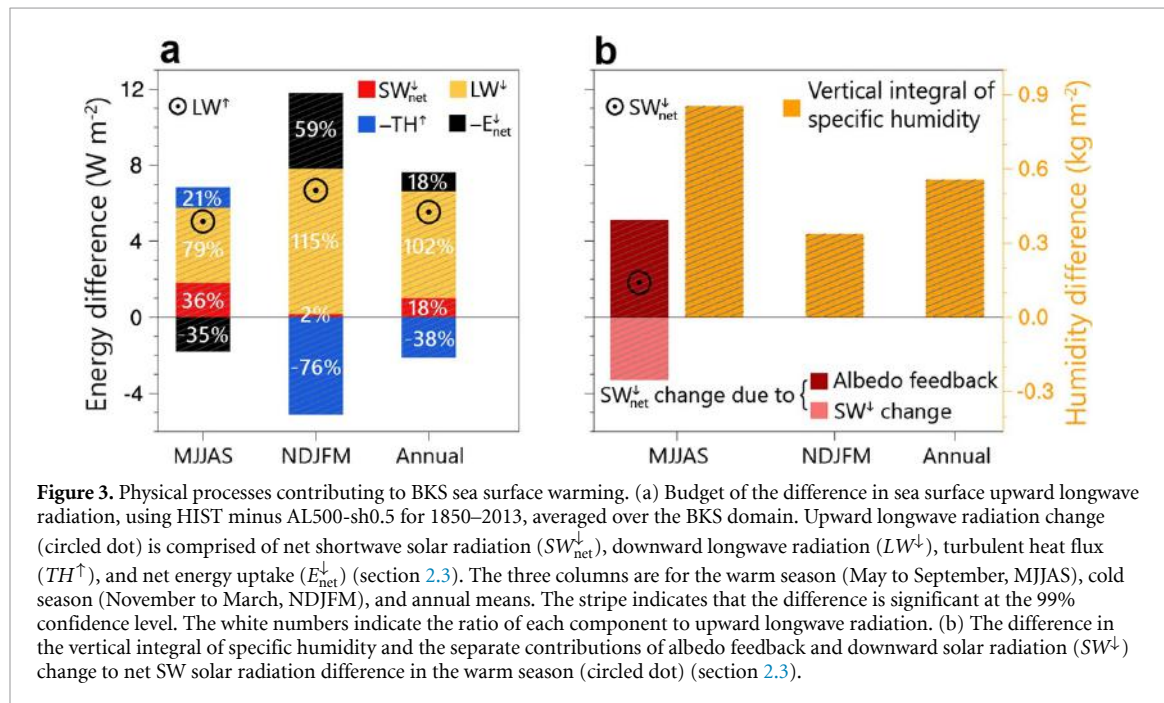


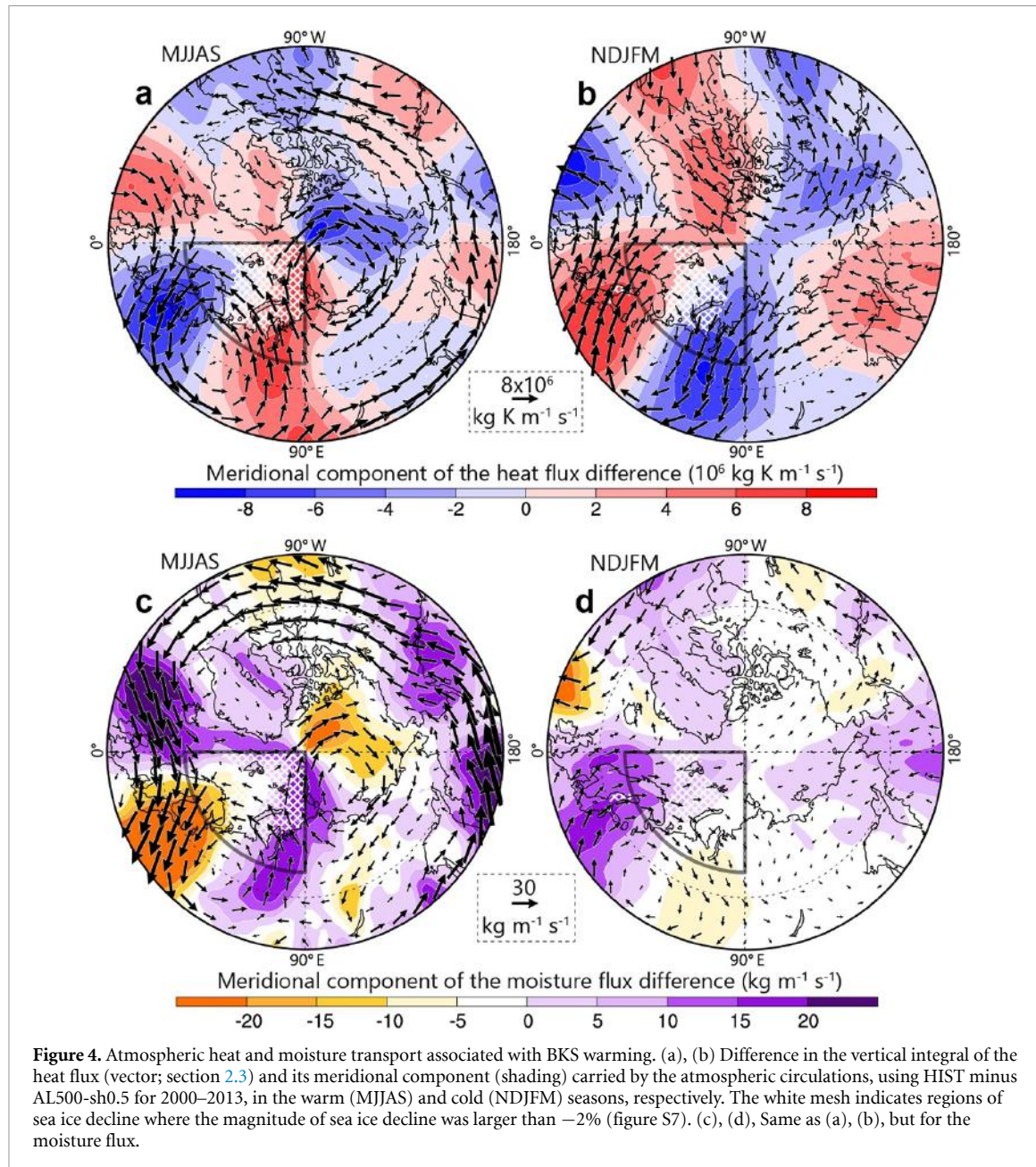
Figure 3. Physical processes contributing to BKS sea surface warming. (a) Budget of the difference in sea surface upward longwave radiation, using HIST minus AL500-sh0.5 for 1850–2013, averaged over the BKS domain. Upward longwave radiation change (circled dot) is comprised of net shortwave solar radiation (SW_{net}^{\downarrow}), downward longwave radiation (LW^{\downarrow}), turbulent heat flux (TH^{\uparrow}), and net energy uptake (E_{net}^{\downarrow}) (section 2.3). The three columns are for the warm season (May to September, MJJAS), cold season (November to March, NDJFM), and annual means. The stripe indicates that the difference is significant at the 99% confidence level. The white numbers indicate the ratio of each component to upward longwave radiation. (b) The difference in the vertical integral of specific humidity and the separate contributions of albedo feedback and downward solar radiation (SW^{\downarrow}) change to net SW solar radiation difference (circled dot) (section 2.3).

3.2. Mechanisms

To determine the mechanisms, the physical processes and large-scale atmospheric circulations that contribute to BKS warming attributable to Asian warming were investigated. The budget of upward LW radiation change was examined because it is another manifestation of the sea surface temperature change according to the Stefan–Boltzmann law (Lu and Cai 2009, Pithan and Mauritsen 2014, Gao *et al* 2019, Xie *et al* 2019, Lesins *et al* 2021). Downward LW radiation made the largest contribution to the upward LW radiation increase for the entire

year (figure 3(a)). However, other processes also had substantial contributions, which varied with the season.

The net energy uptake (local absorption by seawater and external horizontal oceanic heat transport) had a positive contribution in the cold season, accounting for 51% (59%/115%) of the downward LW radiation (figure 3(a)). The TH flux (sensible plus latent) had a negative contribution, and solar radiation was negligible in the cold season due to the long polar nights. In contrast, net energy uptake negatively contributed to upward LW radiation increase in the

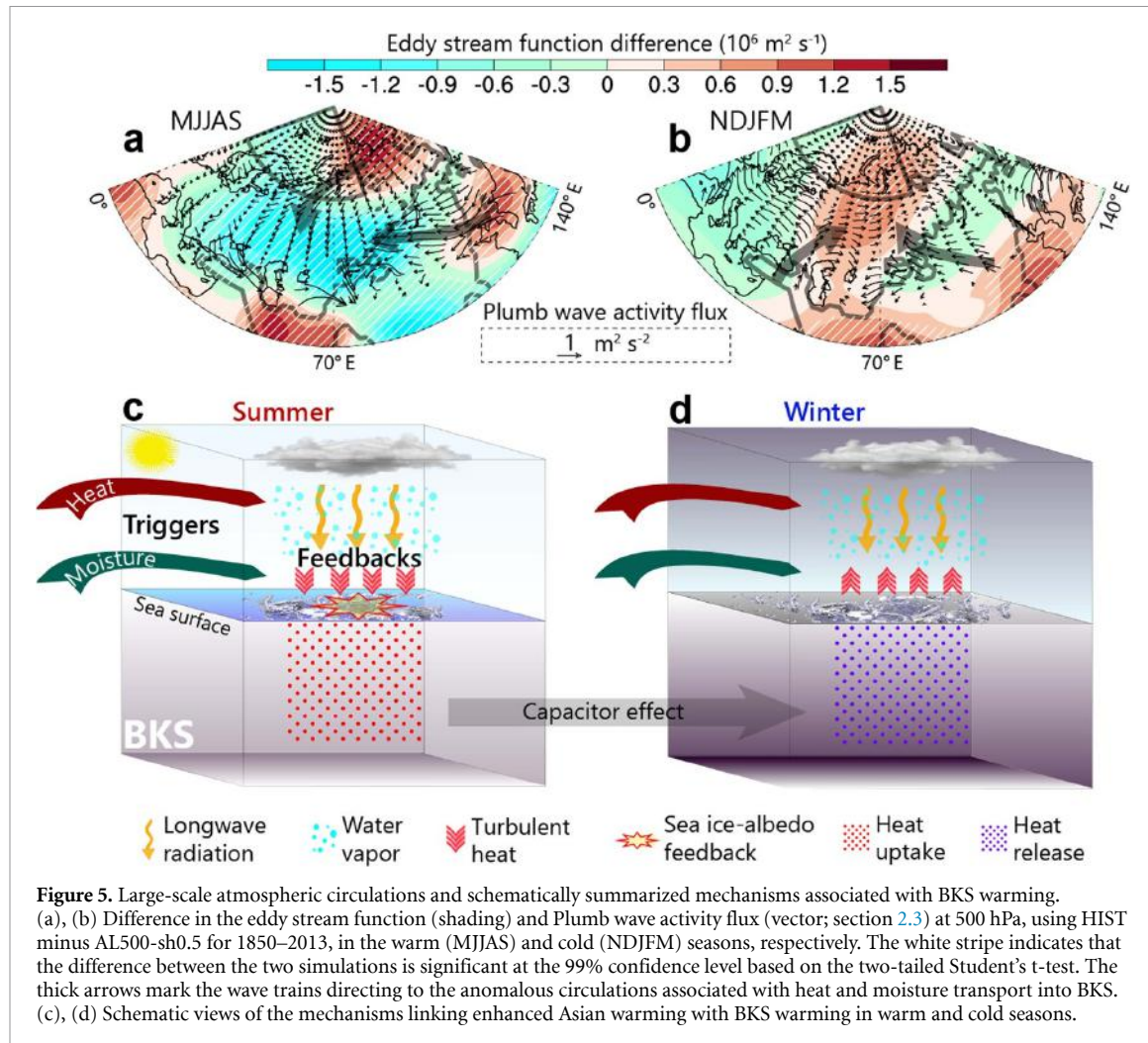


warm season. Net SW solar radiation and TH flux also favored upward LW radiation increase in the warm season. Thus, for BKS sea surface warming, downward LW radiation and net energy uptake had positive contributions in the cold season, in a relative proportion of 7/3. With the relative proportions of 6/3/1, downward LW radiation, net SW solar radiation, and TH flux had positive contributions in the warm season.

Downward LW radiation increase was favored by higher humidity (figures 3(b) and S5) because of the greenhouse effect of water vapor (Gao *et al* 2019, Cai *et al* 2022). Additionally, dense cloud coverage in BKS (figure S6) was another effective factor favoring downward LW radiation in the winter with long polar nights (Xie *et al* 2019). Net energy uptake enhanced the seasonal difference of BKS sea surface

warming by suppressing and strengthening warming in the warm and cold seasons, respectively (Boeke and Taylor 2018). This implies a cross-season energy cycle, which is analogous to the capacitor effect of the ocean (Xie *et al* 2009), charging energy in summer and discharging energy in winter (Xie *et al* 2022a). Net SW solar radiation increase was attributable to the sea ice-albedo feedback (figures 3(b) and S7), which overwhelms the negative contribution of downward solar radiation change due to cloud (He *et al* 2019, Xie *et al* 2022b).

Inputting of external heat or moisture to BKS was required to trigger the downward LW radiation changes and sea ice-albedo feedback. Enhanced heat was transported from lower latitudes into west BKS via the anticyclonic circulation occupying the region to the south of BKS in the cold season (figures 4(b)



and S8). This anticyclonic circulation also transported additional moisture from the south into west BKS (figure 4(d)). The enhanced moisture affected the sea surface temperature via increasing downward LW radiation. Both the enhanced heat and moisture transport occupied the west BKS; however, the enhanced moisture transport extended farther eastward (figures 4(b) and (d)). In particular, the moisture influenced more regions of the strongest warming and sea ice decline (indicated by white mesh) (figures 4(b) and (d)). In addition, the external inputting heat directly affected the air, but not the sea surface, in the cold season because the TH flux was from the sea to the atmosphere (Blackport *et al* 2019). Therefore, the enhanced moisture transport was more important than the transport of heat in favoring BKS warming and sea ice decline in winter.

In contrast to the cold season, cyclonic circulation occurred in the warm season (figures 4(a), (c) and S8). Nonetheless, this cyclonic circulation also favored the heat and moisture input into east BKS from the south (figures 4(a) and (c)), further triggering sea ice-albedo feedback (regions with

white mesh) in the warm season. The enhanced heat transport extended more westward than the enhanced moisture transport (figures 4(a) and (c)); thus, the enhanced heat transport was more important than the enhanced moisture transport in favoring BKS warming and sea ice-albedo feedback in summer. Notably, the enhanced moisture transport was dominant in the BKS moisture increase in the warm season (figures 3(b) and S9(a)) because the local evaporation change in the BKS was weak (figure S9(c)). The local evaporation increase (figure S9(d)), especially in the regions of the strongest warming and sea ice decline (figures 1(b) and 4(d)), was also important for the BKS moisture increase in the cold season (figures 3(b) and S9(b)). In addition, anomalous Rossby wave trains (figures 5(a) and (b)) were responsible for the anomalous atmospheric circulations associated with the heat and moisture flux. Specifically, the two wave trains from downstream and north of AL500 stimulated the anomalous cyclonic circulation in the warm season (figure 5(a)). The wave train downstream AL500 also occurred in the cold season, but it was located more southwestward

(figure 5(b)). Furthermore, a wave train from the west AL500 facilitated anomalous anticyclonic circulation in the cold season (figure 5(b)).

Although the local energy budget is applicable to the sea surface rather than near-surface air, the TH flux and LW radiation connect the sea surface temperature with the near-surface air temperature (figures 5(c) and (d)) (Blackport *et al* 2019, Gao *et al* 2019, Xie *et al* 2019, Cai *et al* 2022). Because TH flux constitutes the energy exchange between air and sea (Blackport *et al* 2019), the negative contribution of TH to sea surface warming in the cold season (figure 3(a)) indicates its positive contribution to near-surface air warming. Therefore, oceanic heat was transported upward to the atmosphere via TH flux in the cold season (figure 5(d)). In contrast, TH suppressed the near-surface air warming (figure 2(a)), but it facilitated oceanic warming in the warm season (figure 5(c)) (Xie *et al* 2022b). Consequently, although the external atmospheric heat input (figures 4(a), (b)) and moisture increase (figure 3(b)) were stronger in the warm season than in the cold season, the near-surface air warming was weak in the warm season (figure 2(a)). Moreover, the capacitor effect of the ocean (Xie *et al* 2022a), i.e. net energy uptake in the warm season and net energy release in the cold season (figures 3(a) and 5(c), (d)), relied on the TH flux.

4. Conclusions and discussion

This study revealed a new factor underlying the Arctic amplification, as well as a new climatic influence of the enhanced Asian warming. The enhanced Asian warming includes the warming over the Asian dryland (Huang *et al* 2016a, 2017, Xie *et al* 2019) and Tibetan Plateau (Duan and Xiao 2015, Yao *et al* 2019, You *et al* 2020). The Tibetan Plateau is recognized as the third pole (Qiu 2008, Barry and Hall-McKim 2018) on Earth (in addition to the North Pole and South Pole). An influence of the Arctic on the Tibetan Plateau has recently been proposed (Li *et al* 2020, Duan *et al* 2022). Here, we further demonstrated an influence of the Tibetan Plateau on the Arctic. These results imply potential pole-to-pole interactions between the Arctic and the third pole. Therefore, our findings prompt future research on pole-to-pole interactions. In addition to the local environmental influence, we argue that the influences of dryland climate change on remote regions should be considered carefully, especially under accelerated dryland expansion and warming (Feng and Fu 2013, Huang *et al* 2016b, 2017, Xie *et al* 2019).

The mechanisms underlying the connections between Asian warming and BKS warming were schematically summarized in figures 5(c) and (d). Asian warming exerted its influence on BKS by inducing anomalous circulations that transported external heat and moisture into BKS. As triggers,

the external heat and moisture stimulated local feedbacks; the heat directly influences temperature, while the moisture influences temperature by its greenhouse effect associated with LW radiation. The LW radiation increase made the largest contributions to the BKS warming in both summer and winter. The sea ice-albedo feedback also made a crucial contribution to BKS warming in summer. Because of the capacitor effect of the ocean, the ocean acquired energy in summer and released the energy in winter. Therefore, the cross-season energy cycles due to the oceanic capacitor effect suppressed the summer warming but promoted the winter warming in the BKS, in which the TH flux was the main pathway exchanging heat between ocean and atmosphere. In addition, as two components of enhanced Asian warming, the Tibetan Plateau and dryland (averaged over the AL500 regions higher than 2 km or not, respectively), had warming magnitudes of 1.7 °C and 1.3 °C in simulations (figure 1(b)). Therefore, the Tibetan Plateau warming may have a larger influence on the BKS warming than dryland, as inferred from the perspective of linear superposition. However, the individual effects of the Tibetan Plateau and dryland and their possible interactions will be investigated in future studies. In addition to SH, other factors, such as changes in surface albedo over the Tibetan Plateau and downward LW radiation over the dryland, have also influenced the HIST warming over the AL500 (Ma *et al* 2017, Gao *et al* 2019, Xie *et al* 2019, You *et al* 2021). Therefore, more experiments were expected to verify our results based on the SH-modification method in future studies.

Data availability statement

ERA5 data are available from www.ecmwf.int/en/forecasts/datasets/reanalysis-datasets/era5. PREC/L data are available from <https://psl.noaa.gov/data/gridded/data.precl.html>. CRU data are available from https://data.ceda.ac.uk/badc/cru/data/cru_ts/cru_ts_4.05. The codes of CESM experiments are available at <https://doi.org/10.5281/zenodo.7523621>.

Acknowledgments

We thank the anonymous reviewers for their constructive comments. We thank Bian He for his comments. We thank the CESM Working Groups, NCAR/UCAR, for providing the CESM model, and the National Supercomputing Center in Wuxi, China, for providing technical support during CESM2.1.3 porting. We also thank the ECMWF, NOAA PSL, and CRU for making their data available. This work was supported by the National Natural Science Foundation of China (91937302, 42030602) and Gansu Provincial Special Fund Project for Guiding Scientific and Technological Innovation and Development (2019ZX-06).

Conflict of interest

Authors declare that they have no competing interests.

ORCID iD

Jianping Huang  <https://orcid.org/0000-0003-2845-797X>

References

Allen R G, Pereira L S, Raes D and Smith M 1998 Crop evapotranspiration—guidelines for computing crop water requirements *FAO Irrigation and drainage paper* Paper 56 (Rome: Food and Agricultural Organization of the United Nations)

Bao Y, Song Z and Qiao F 2020 FIO-ESM version 2.0: model description and evaluation *J. Geophys. Res.* **125** e2019JC016036

Barry R and Hall-McKim E 2018 The third pole *Polar Environments and Global Change* (Cambridge: Cambridge University Press) pp 339–77

Benjamini Y and Hochberg Y 1995 Controlling the false discovery rate: a practical and powerful approach to multiple testing *J. R. Stat. Soc. B* **57** 289–300

Blackport R, Screen J A, van der Wiel K and Bintanja R 2019 Minimal influence of reduced Arctic sea ice on coincident cold winters in mid-latitudes *Nat. Clim. Change* **9** 697–704

Boeke R C and Taylor P C 2018 Seasonal energy exchange in sea ice retreat regions contributes to differences in projected Arctic warming *Nat. Commun.* **9** 5017

Cai M 2005 Dynamical amplification of polar warming *Geophys. Res. Lett.* **32** L22710

Cai Z, You Q, Chen H W, Zhang R, Chen D L, Chen J, Kang S and Cohen J 2022 Amplified wintertime Barents Sea warming linked to intensified Barents oscillation *Environ. Res. Lett.* **17** 044068

Chen M, Xie P, Janowiak J E and Arkin P A 2002 Global land precipitation: a 50-yr monthly analysis based on gauge observations *J. Hydrometeorol.* **3** 249–66

Cohen J et al 2019 Divergent consensuses on Arctic amplification influence on midlatitude severe winter weather *Nat. Clim. Change* **10** 20–29

Dai A, Luo D, Song M and Liu J 2019 Arctic amplification is caused by sea-ice loss under increasing CO₂ *Nat. Commun.* **10** 121

Danabasoglu G et al 2020 The community earth system model version 2 (CESM2) *J. Adv. Model. Earth Syst.* **12** e2019MS001916

Delworth T L, Zeng F, Vecchi G A, Yang X, Zhang L and Zhang R 2016 The North Atlantic oscillation as a driver of rapid climate change in the Northern Hemisphere *Nat. Geosci.* **9** 509–12

Ding Q et al 2018 Fingerprints of internal drivers of Arctic sea ice loss in observations and model simulations *Nat. Geosci.* **12** 28–33

Duan A, Peng Y, Liu J, Chen Y, Wu G, Holland D M, He B, Hu W, Tang Y and Li X 2022 Sea ice loss of the Barents-Kara Sea enhances the winter warming over the Tibetan Plateau *npj Clim. Atmos. Sci.* **5** 26

Duan A and Xiao Z 2015 Does the climate warming hiatus exist over the Tibetan Plateau? *Sci. Rep.* **5** 13711

Eyring V, Bony S, Meehl G A, Senior C A, Stevens B, Stouffer R J and Taylor K E 2016 Overview of the coupled model intercomparison project phase 6 (CMIP6) experimental design and organization *Geosci. Model Dev.* **9** 1937–58

Feng S and Fu Q 2013 Expansion of global drylands under a warming climate *Atmos. Chem. Phys.* **13** 10081–94

Gao K, Duan A, Chen D and Wu G 2019 Surface energy budget diagnosis reveals possible mechanism for the different warming rate among Earth's three poles in recent decades *Sci. Bull.* **64** 1140–3

Gillet N P, Stone D A, Stott P A, Nozawa T, Karpechko A Y, Hegerl G C, Wehner M F and Jones P D 2008 Attribution of polar warming to human influence *Nat. Geosci.* **1** 750–4

Graversen R and Burtu M 2016 Arctic amplification enhanced by latent energy transport of atmospheric planetary waves *Q. J. R. Meteorol. Soc.* **142** 2046–54

Harris I C, Osborn T J, Jones P D and Lister D H 2020 Version 4 of the CRU TS monthly high-resolution gridded multivariate climate dataset *Sci. Data* **7** 109

He B et al 2020 CAS FGOALS-f3-L model datasets for CMIP6 GMMIP Tier-1 and Tier-3 experiments *Adv. Atmos. Sci.* **37** 18–28

He M, Hu Y, Chen N, Wang D, Huang J and Stammes K 2019 High cloud coverage over melted areas dominates the impact of clouds on the albedo feedback in the Arctic *Sci. Rep.* **9** 9529

Hersbach H et al 2020 The ERA5 global reanalysis *Q. J. R. Meteorol. Soc.* **146** 1999–2049

Huang J, Guan X and Ji F 2012 Enhanced cold-season warming in semi-arid regions *Atmos. Chem. Phys.* **12** 5391–8

Huang J, Ji M, Xie Y, Wang S, He Y and Ran J 2016a Global semi-arid climate change over last 60 years *Clim. Dyn.* **46** 1131–50

Huang J, Yu H, Dai A, Wei Y and Kang L 2017 Drylands face potential threat under 2 °C global warming target *Nat. Clim. Change* **7** 417–22

Huang J, Yu H, Guan X, Wang G and Guo R 2016b Accelerated dryland expansion under climate change *Nat. Clim. Change* **6** 166–71

IPCC 2021 Summary for policymakers *Climate Change 2021: The Physical Science Basis. Contribution of Working Group I to the Sixth Assessment Report of the Intergovernmental Panel on Climate Change* ed V Masson-Delmotte et al (Cambridge: Cambridge University Press) pp 3–32

Kosaka Y and Xie S 2013 Recent global-warming hiatus tied to equatorial Pacific surface cooling *Nature* **501** 403–7

Kretschmer M, Coumou D, Donges J F and Runge J 2016 Using causal effect networks to analyze different arctic drivers of midlatitude winter circulation *J. Clim.* **29** 4069–81

Lesins G, Duck T J and Drummond J R 2012 Surface energy balance framework for Arctic Amplification of climate change *J. Clim.* **25** 8277–88

Li F, Wan X, Wang H, Orsolini Y J, Cong Z, Gao Y and Kang S 2020 Arctic sea-ice loss intensifies aerosol transport to the Tibetan Plateau *Nat. Clim. Change* **10** 1037–44

Lin P, Yu Z, Lü J, Ding M, Hu A and Liu H 2019 Two regimes of Atlantic multidecadal oscillation: cross-basin dependent or Atlantic-intrinsic *Sci. Bull.* **64** 198–204

Liu Y, Hoskins B J and Blackburn M 2007 Impact of Tibetan orography and heating on the summer flow over Asia *J. Meteorol. Soc. Jpn.* **85** 1–19

Lu J and Cai M 2009 Seasonality of polar surface warming amplification in climate simulations *Geophys. Res. Lett.* **36** L16704

Lu M, Yang S, Li Z, He B, He S and Wang Z 2018 Possible effect of the Tibetan Plateau on the “upstream” climate over West Asia, North Africa, South Europe and the North Atlantic *Clim. Dyn.* **51** 1485–98

Luo B, Luo D, Wu L, Zhong L and Simmonds I 2017 Atmospheric circulation patterns which promote winter Arctic sea ice decline *Environ. Res. Lett.* **12** 054017

Ma J, Guan X, Guo R, Gan Z and Xie Y 2017 Mechanism of non-appearance of hiatus in Tibetan Plateau *Sci. Rep.* **7** 4421

Mantua N J and Hare S R 2002 The Pacific decadal oscillation *J. Oceanogr.* **58** 35–44

Pithan F and Mauritsen T 2014 Arctic amplification dominated by temperature feedbacks in contemporary climate models *Nat. Geosci.* **7** 181–4

Plumb R A 1985 On the three-dimensional propagation of stationary waves *J. Atmos. Sci.* **42** 217–29

Qiu J 2008 China: the third pole *Nature* **454** 393–6

Rodell M *et al* 2004 The global land data assimilation system *Bull. Am. Meteorol. Soc.* **85** 381–94

Screen J A and Simmonds I 2010 The central role of diminishing sea ice in recent Arctic temperature amplification *Nature* **464** 1334–7

Smith D M *et al* 2019 The polar amplification model intercomparison project (PAMIP) contribution to CMIP6: investigating the causes and consequences of polar amplification *Geosci. Model Dev.* **12** 1139–64

Stouffer R J and Manabe S 2017 Assessing temperature pattern projections made in 1989 *Nat. Clim. Change* **7** 163–5

Svendsen L, Keenlyside N S, Bethke I, Gao Y and Omrani N 2018 Pacific contribution to the early twentieth-century warming in the Arctic *Nat. Clim. Change* **8** 793–7

Trenberth K E 2015 Has there been a hiatus? *Science* **349** 691–2

Wang B, Bao Q, Hoskins B, Wu G and Liu Y 2008 Tibetan Plateau warming and precipitation changes in East Asia *Geophys. Res. Lett.* **35** L14702

Wang M, Wang J, Chen D, Duan A, Liu Y, Zhou S, Guo D, Wang H and Ju W 2019 Recent recovery of the boreal spring sensible heating over the Tibetan Plateau will continue in CMIP6 future projections *Environ. Res. Lett.* **14** 124066

Wu G, Liu Y, He B, Bao Q, Duan A and Jin F 2012 Thermal controls on the Asian summer monsoon *Sci. Rep.* **2** 404

Wu G, Liu Y, Wang T, Wan R, Liu X, Li W, Wang Z, Zhang Q, Duan A and Liang X 2007 The influence of mechanical and thermal forcing by the Tibetan Plateau on Asian climate *J. Hydrometeorol.* **8** 770–89

Wu G, Zhuo H, Wang Z and Liu Y 2016 Two types of summertime heating over the Asian large-scale orography and excitation of potential-vorticity forcing I. over Tibetan Plateau *Sci. China Earth Sci.* **59** 1996–2008

Xie S, Hu K, Hafner J, Tokinaga H, Du Y, Huang G and Sampe T 2009 Indian Ocean capacitor effect on Indo–Western Pacific climate during the summer following El Niño *J. Clim.* **22** 730–47

Xie Y, Huang J and Ming Y 2019 Robust regional warming amplifications directly following the anthropogenic emission *Earth's Future* **7** 363–9

Xie Y, Nie H and He Y 2022a Extratropical climate change during periods before and after an Arctic ice-free summer *Earth's Future* **10** e2022EF002881

Xie Y, Wu G, Liu Y and Huang J 2020 Eurasian cooling linked with Arctic warming: insights from PV dynamics *J. Clim.* **33** 2627–44

Xie Y, Wu G, Liu Y, Huang J and Nie H 2022b A dynamic and thermodynamic coupling view of the linkages between Eurasian cooling and Arctic warming *Clim. Dyn.* **58** 2725–44

Xie Y, Wu G, Liu Y, Huang J, Sheng C and Wu Y 2023 A potential vorticity budget view of the atmospheric circulation climatology over the Tibetan Plateau *Int. J. Climatol.* accepted (<https://doi.org/10.1002/joc.7960>)

Yanai M, Li C W and Song Z 1992 Seasonal heating of the Tibetan Plateau and its effects on the evolution of the Asian summer monsoon *J. Meteorol. Soc. Jpn.* **70** 319–51

Yang H, Shen X, Yao J and Wen Q 2020 Portraying the impact of the Tibetan Plateau on global climate *J. Clim.* **33** 3565–83

Yao T *et al* 2019 Recent third pole's rapid warming accompanies cryospheric melt and water cycle intensification and interactions between monsoon and environment: multidisciplinary approach with observations, modeling, and analysis *Bull. Am. Meteorol. Soc.* **100** 423–44

You Q *et al* 2021 Warming amplification over the Arctic pole and third pole: trends, mechanisms and consequences *Earth-Sci. Rev.* **217** 103625

You Q, Chen D, Wu F, Pepin N C, Cai Z, Ahrens B, Jiang Z, Wu Z, Kang S and Aghakouchak A 2020 Elevation dependent warming over the Tibetan Plateau: patterns, mechanisms and perspectives *Earth-Sci. Rev.* **210** 103349

Zhou T, Turner A G, Kinter J L, Wang B, Qian Y, Chen X, Wu B, Liu B, Zou L and He B 2016 GMMIP (v1.0) contribution to CMIP6: global monsoons model inter-comparison project *Geosci. Model Dev.* **9** 3589–604

Supplementary material

Enhanced Asian warming increases Arctic amplification

Yongkun Xie¹, Jianping Huang¹, Guoxiong Wu^{2,3}, Nan Lei^{1,4}, and Yimin Liu^{2,3}

¹ Collaborative Innovation Center for Western Ecological Safety, Lanzhou University, Lanzhou, China.

² State Key Laboratory of Numerical Modeling for Atmospheric Sciences and Geophysical Fluid Dynamics (LASG), Institute of Atmospheric Physics, Chinese Academy of Sciences, Beijing, China

³ College of Earth and Planetary Sciences, University of Chinese Academy of Sciences, Beijing, China

⁴ College of Atmospheric Sciences, Lanzhou University, Lanzhou, China.

Contents of this file:

Figures S1 to S9

Tables S1

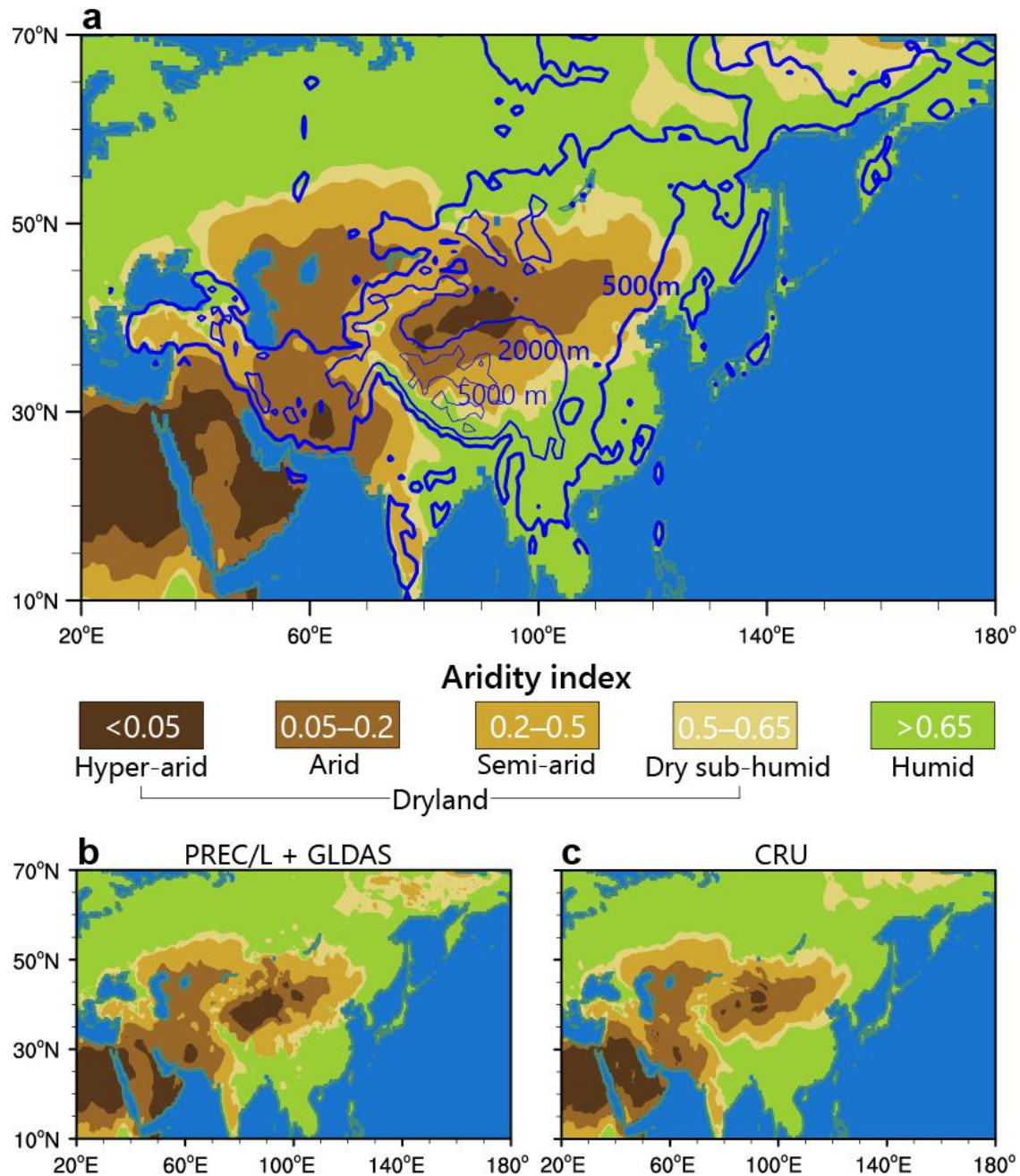


Figure S1. (a), Distribution of Asian dryland and Asian land above 500 m (AL500). Asian dryland was identified by an aridity index value less than 0.65. The aridity index was the average of the results based on the (b), PREC/L and GLDAS datasets and (c), CRU dataset for the period from 1971 to 2000. The domain of AL500 is marked by the thickest blue contour. The other two contours indicate the 2000 m and 5000 m elevations, respectively.

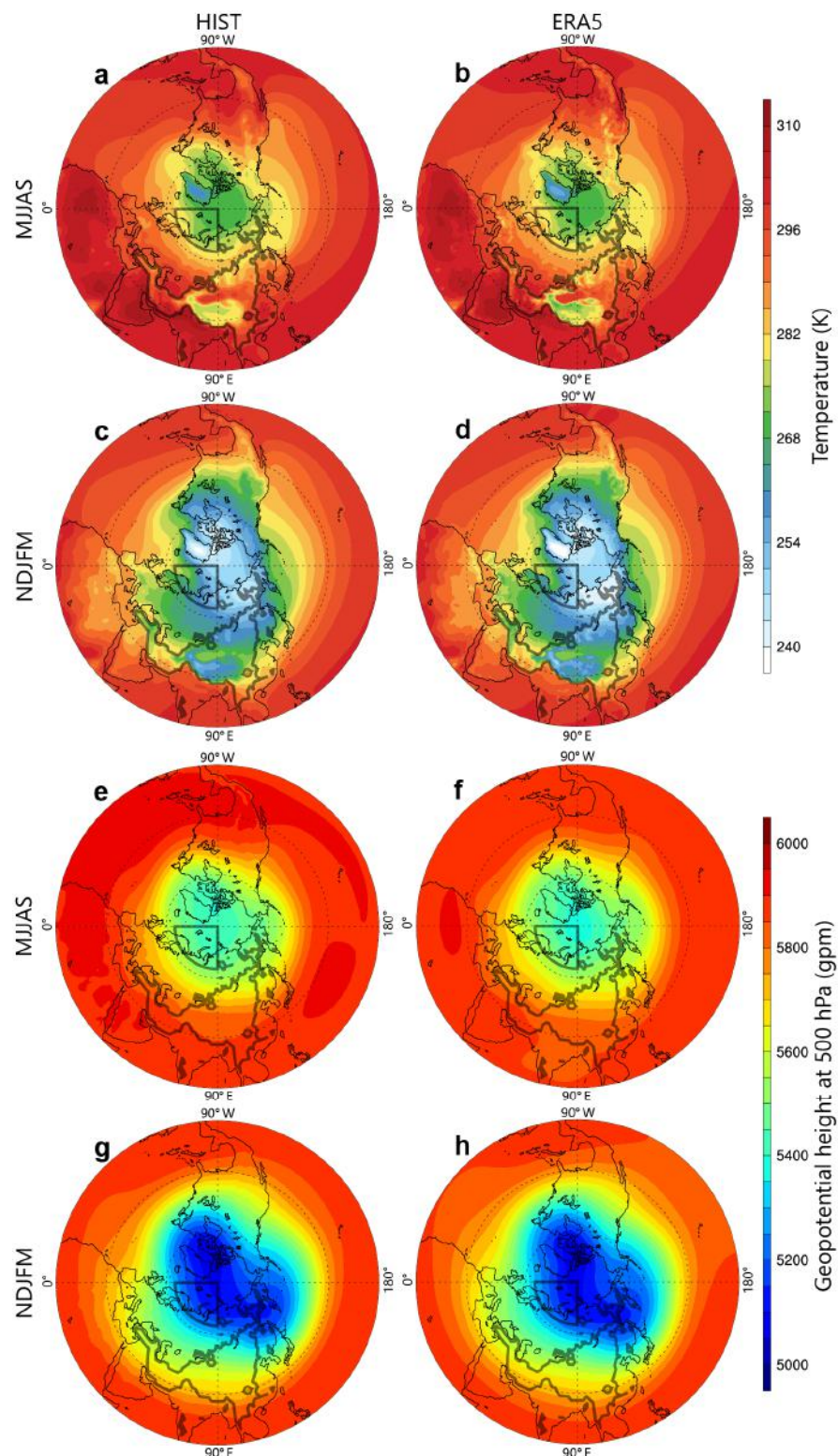


Figure S2. Climatology of (a–d), near-surface air temperature and (e–h), geopotential height at 500 hPa for the period from 1950 to 2013. The results were for (a, b, e, f), warm and (c, d, g, h), cold seasons based on (left), HIST simulation and (right), ERA5 data.

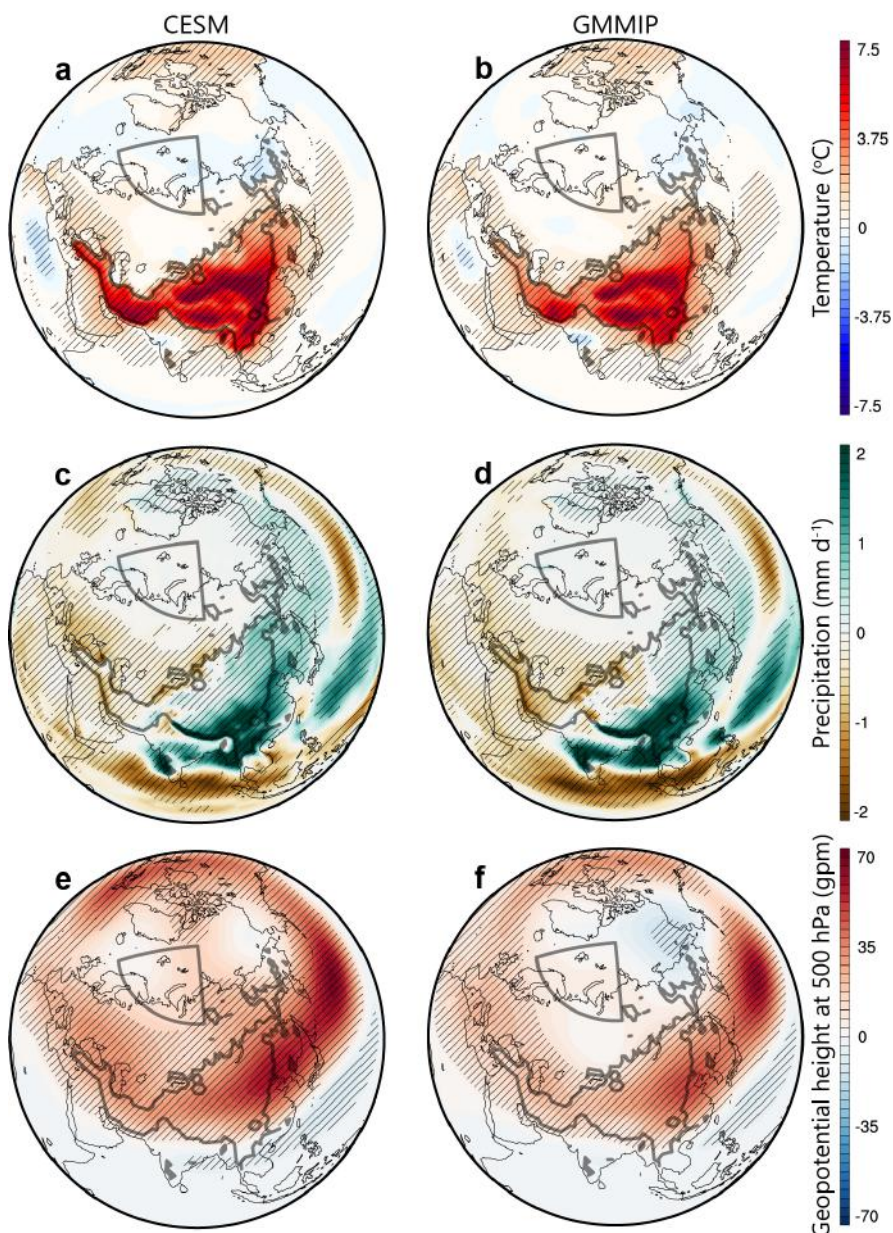


Figure S3. Difference in annual mean near-surface air temperature for 1979–2014 determined using amip-HIST minus amip-AL500-sh0.5 simulations for (a), CESM and (b), GMMIP results. The GMMIP results were the average of FGOALS-f3-L and FIO-ESM-2-0. The stripe indicates that the difference between the two simulations is significant at the 99% confidence level based on the two-tailed Student's t-test. (c, d) and (e, f), Same as (a, b) but for precipitation and geopotential height at 500 hPa, respectively.

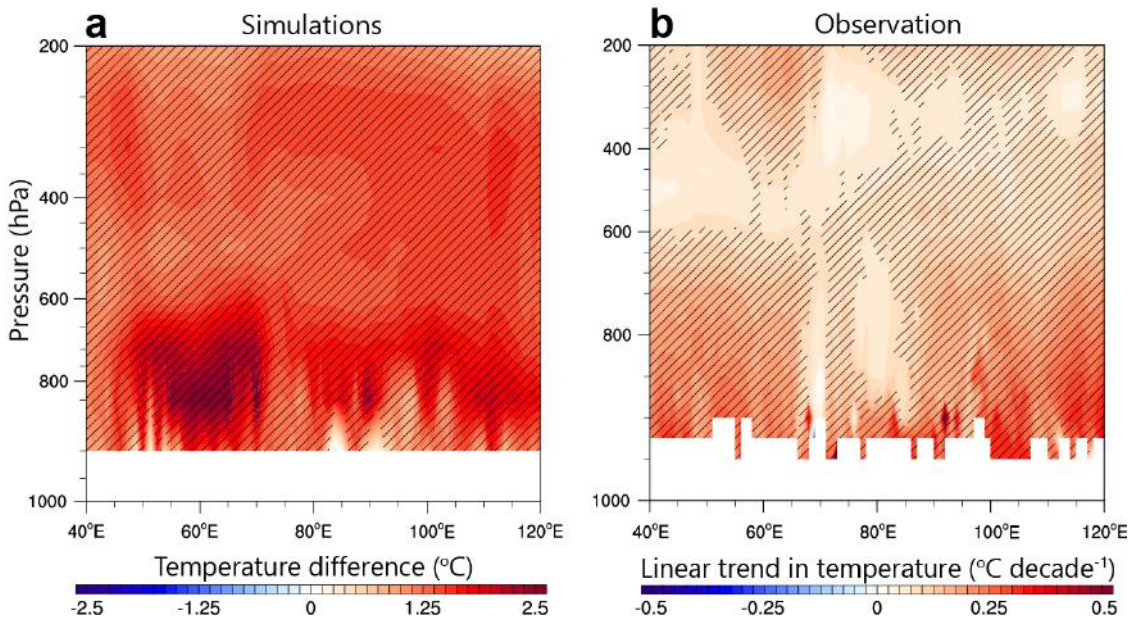


Figure S4. (a), Vertical–latitudinal cross-section (averaged over 25°–60°N of AL500) of the difference in annual mean temperature for 1850–2014 determined using HIST minus AL500-sh0.5 simulations. The stripe indicates that the difference between the two simulations is significant at the 99% confidence level based on the two-tailed Student’s t-test. (b), Same as (a) but for linear trend in annual mean temperature during 1950–2021 based on ERA5 data. The stripe indicates that the linear trend is significant at the 99% confidence level based on the two-tailed Student’s t-test and FDR-adjusted P -values.

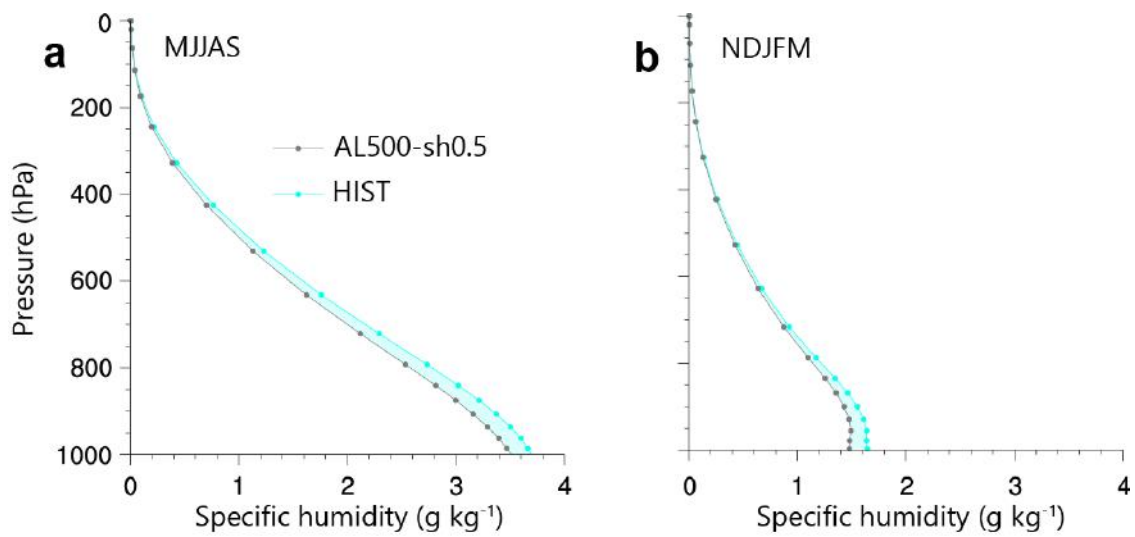


Figure S5. Vertical profiles of specific humidity averaged over the BKS for (a), warm and (b), cold seasons for 1850–2013, from the HIST (turquoise) and AL500-sh0.5 (gray) simulations, respectively. The filled turquoise color indicates that the BKS humidity difference determined using HIST minus AL500-sh0.5 was positive.

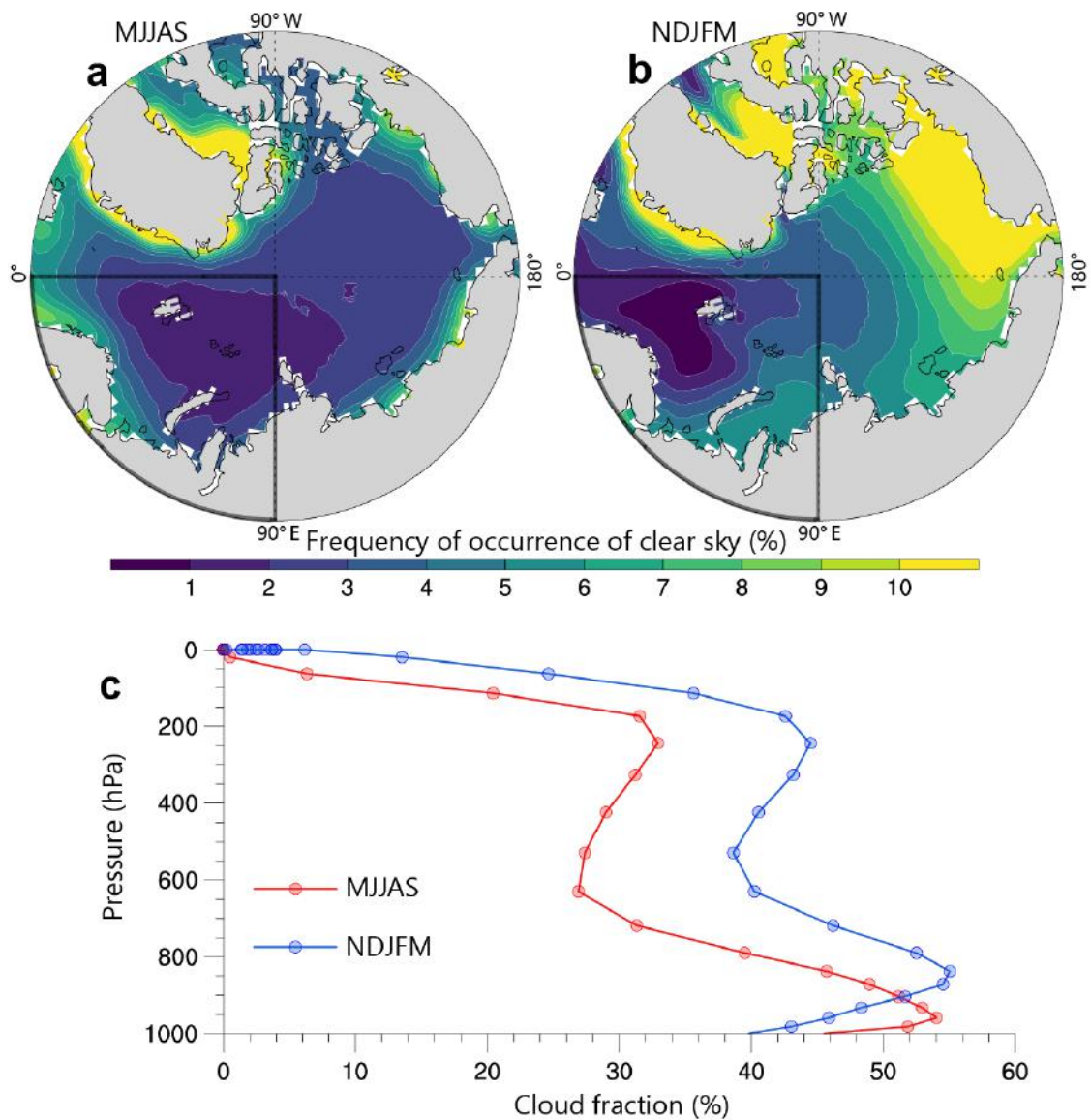


Figure S6. Climatological mean frequency of occurrence of clear sky in (a), warm and (b), cold seasons from the HIST simulation for 1850–2013. (c), Vertical profile of cloud fraction averaged over the BKS from the HIST simulation.

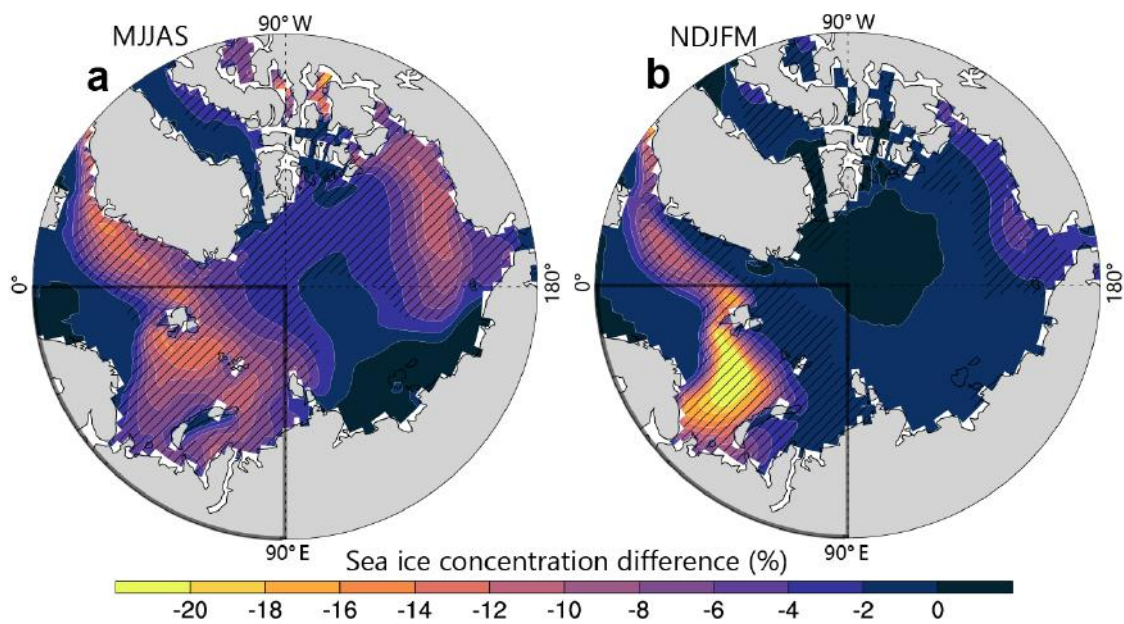


Figure S7. Difference in sea ice concentration determined using HIST minus AL500-sh0.5 simulations for (a), warm and (b), cold seasons for 1850–2013. The stripe indicates that the difference is significant at the 99% confidence level based on the two-tailed Student's t-test.

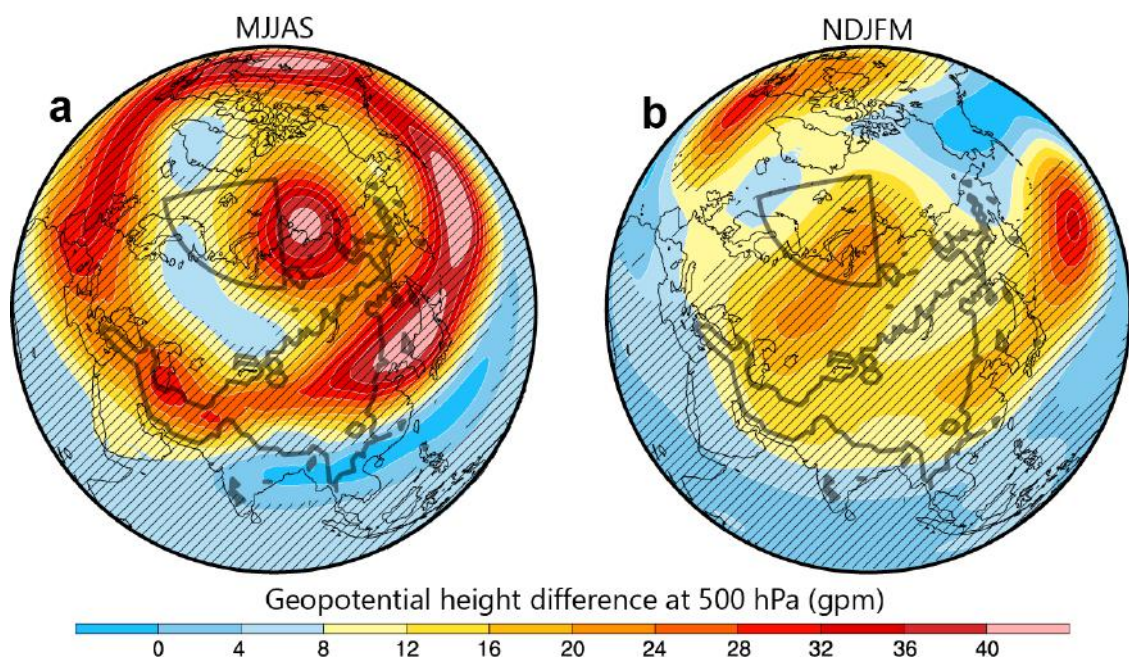


Figure S8. Difference in geopotential height at 500 hPa for (a), warm and (b), cold seasons determined using HIST minus AL500-sh0.5 for 1850–2013. The stripe indicates that the difference is significant at the 99% confidence level based on the two-tailed Student's t-test.

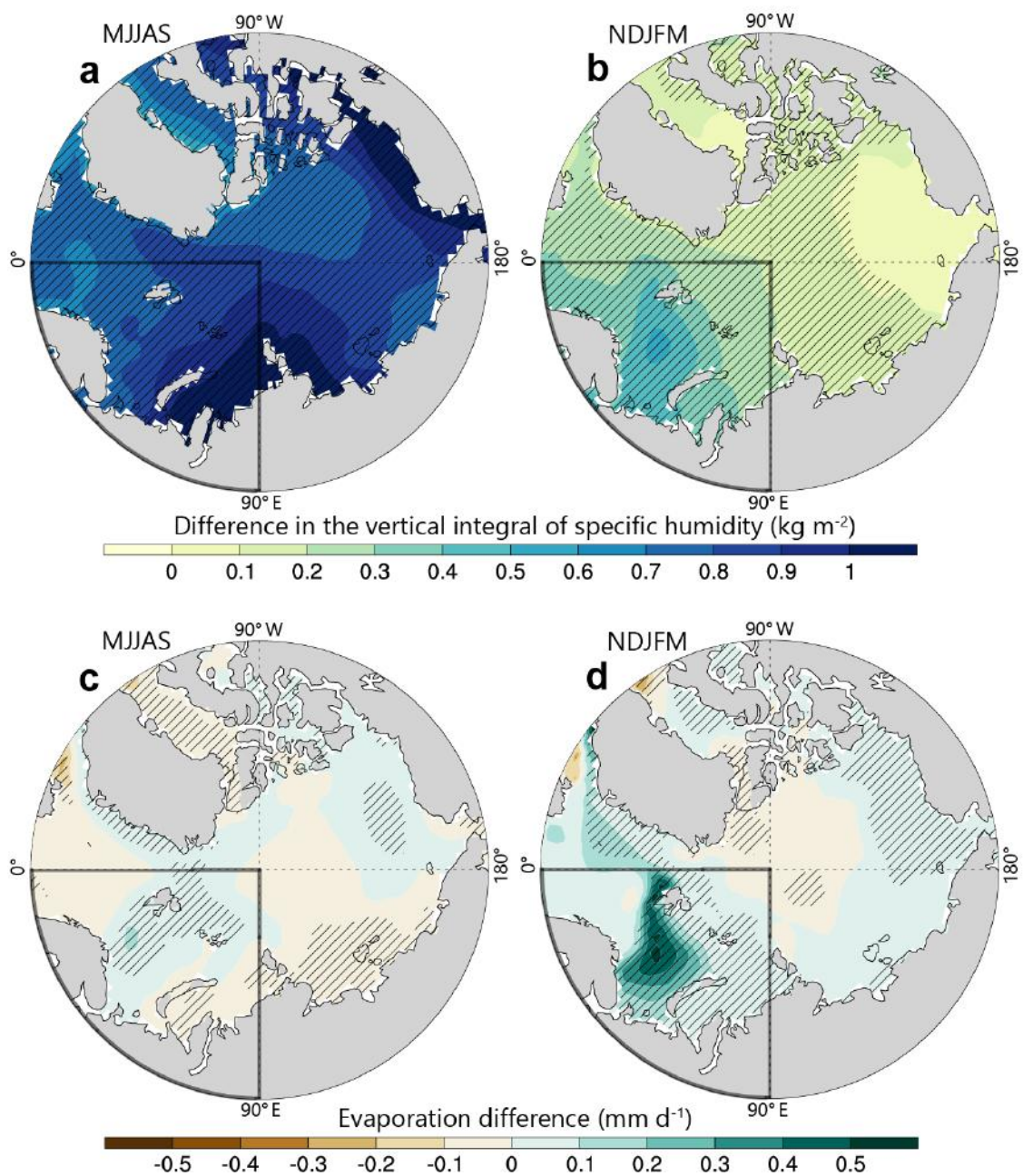


Figure S9. Difference in the vertical integral of specific humidity for (a), warm and (b), cold seasons determined using HIST minus AL500-sh0.5 simulations for 1850–2013. The stripe indicates that the difference is significant at the 99% confidence level based on the two-tailed Student's t-test. (c, d), Same as (a, b) but for sea surface evaporation.

Table S1. Experimental designs and models. This study performed the CESM experiments, while CMIP6 provided the output of GMMIP experiments. The amip-labeled experiments were atmosphere-only simulations using atmospheric circulation models without ocean coupling. The other experiments used fully coupled climate models.

| CESM Experiments | | | |
|-------------------|---|----------------------------|-------------------------|
| Name | Design | Time | |
| HIST | The control run was the benchmark CMIP6 historical (HIST) simulation, with external forcing defined by the observed values. The number of ensemble integrations was 1. Modified from the official case ¹ : BHIST. | 1850/01 | — |
| AL500-sh0.5 | The sensitivity run was modified from HIST. The heating of Asian land above 500 m (AL500) was modified by halving the sensible heat of the entire column of the atmosphere. The number of ensemble integrations was 1. | 2014/12 | — |
| amip-HIST | Same as HIST but for atmosphere-only simulation and a different integration time. The number of ensemble integrations was 1. Modified from the official case: FHIST. | 1979/01 | — |
| amip-AL500-nosh | Same as AL500-sh0.5 but for atmosphere-only simulation, a different integration time, and removing sensible heat instead of halving. The number of ensemble integrations was 1. | 2014/12 | — |
| CMMIP Experiments | | | |
| Name | Design | Models | Time |
| amip-HIST | Same as amip-HIST of CESM but for a different integration time. Its GMMIP tag was amip-hist. The number of ensemble integrations was 3. | FGOALS-f3-L FIO-ESM-2-0 | 1861/01 — 2014/12 |
| amip-AL500-nosh | Same as amip-AL500-nosh of CESM but for a different integration time. Its GMMIP tag was amip-TIP-nosh. TIP indicates the Tibetan–Iranian Plateau coupling system. The number of ensemble integrations was 1. | | 1870/01 — 2014/12 |

Models

| Name | Resolution | Institute |
|-------------------------|--|------------------------|
| CESM (version 2.1.3) | Official tag ² : f09_g17 Atmos: CAM6, 0.9×1.25 finite volume grid, 32 vertical levels Land: CLM5.0, 0.9×1.25 finite volume grid Ocean: POP2, finite volume grid $0.9 \times 1.25_g \times 1v7$ | NCAR/ UCAR/ USA |
| FGOALS-f3-L | Atmos: FAMIL2.2, c96 finite volume grid; 180×360 lat/lon; 32 vertical levels | IAP- LASG/ China |
| FIO-ESM-2-0 | Atmos: CAM4, 0.9×1.25 finite volume grid; 192×288 lat/lon; 26 vertical levels | FIO/ China |

¹ <https://www2.cesm.ucar.edu/models/cesm2/config/2.1.3/compsets.html>

² <https://www2.cesm.ucar.edu/models/cesm2/config/2.1.3/grids.html>